Sustainable Chemical Engineering
https://ojs.wiserpub.com/index.php/SCE/

UNIVERSAL WISER PUBLISHER

Research Article

Impact of Sn-Doped Zn_3P_2 Nanopowders: Structural, Optical, and Photoluminescence Studies

Nakka Praveenkumar[1], Nasina Madhusudhana Rao[2], Mathew K. Moodley[1*], S.V. Motloung Setumo[3]

[1]Discipline of Physics, University of KwaZulu-Natal, Westville Campus, Private Bag X54001, Durban, 4000, South Africa
[2]Department of Physics, School of Advanced Sciences, VIT-AP University, Inavolu, Beside AP Secretariat, Amaravati, Andhra Pradesh, 522237, India
[3]Directorate, Postgraduate Studies, Central University of Technology, Private Bag X 20539, Bloemfontein, 9300, South Africa
E-mail: moodleymk@ukzn.ac.za

Received: 9 February 2026; **Revised:** 15 April 2026; **Accepted:** 17 April 2026

Abstract: A solid-state method was used to create diluted magnetic semiconductor nanoparticles doped with Sn. These nanoparticles have the formula $Zn_{3-x}Sn_xP_2$, where x = 0.03, 0.05, and 0.09. The impact of Sn-dopant concentration on the optical, photoluminescent, and structural characteristics of artificial samples was investigated. The samples were created with a tetragonal structure, according to the X-ray diffraction study, and the diffraction peaks showed no additional Sn or impurities. As the Sn concentration rose, the lattice parameters changed from $a = b$ = 8.1093 to 8.1431 Å and c = 11.1193 Å to 11.1398 Å. As the dopant level increased, the nanoparticles tended to clump together in the 500 nm region, according to scanning electron microscope images. The energy-dispersive X-ray spectroscopy study indicates that this dopant concentration is close to the required Sn, P, and Zn atomic ratios. UV-visible-near-infrared spectroscopy and photoluminescence tests were used to study the optical characteristics. With an increase in Sn concentration, the optical band gap grew from 1.422 eV to 1.432 eV. The examination of photoluminescence revealed emissions in the blue, violet, and ultraviolet bands.

***Keywords*:** II-V alloy, Sn-doped Zn_3P_2, room temperature, elemental composition, photoluminescence studies

1. Introduction

Spintronics, an emerging field in nanoscale electronics that leverages the spin of electrons alongside their charge for data processing and storage, is feasible with the use of Dilute Magnetic Semiconductors (DMS). Investigations into spintronics, leveraging the spin property of electrons, are currently in progress.[1] Every DMS material exhibits distinct characteristics and applications in magneto-optical and magneto-transport systems.[2] DMSs exhibit semimagnetic properties. A DMS consists of a combination of magnetic and non-magnetic materials, whereas a conventional magnetic semiconductor features magnetic components that are arranged in a periodic manner. These definitions are crucial for grasping their unique characteristics. Recently, there has been a significant increase in the interest in advanced fields, including magnetoelectronics, magneto-optoelectronics, and spintronics, with a particular focus on transition metal ion-doped oxide DMS.[3] Research has focused on compounds that include III-V and IV-VI types of magnetic

Copyright ©2026 Mathew K. Moodley, et al.
DOI: https://doi.org/10.37256/sce.7220269762
This is an open-access article distributed under a CC BY license
(Creative Commons Attribution 4.0 International License)
https://creativecommons.org/licenses/by/4.0/

semiconductors, in contrast to those of the II-V category. This semiconductor material, which does not exhibit magnetic properties, can be enhanced through magnetic doping with transition metals such as Mn, Fe, Ni, and V, as well as rare earth metals like Gd and Dy.

Zinc Phosphide (Zn_3P_2) is an environmentally friendly, polar, mixed-valent material that belongs to the class of II-V semiconductors and is also cost-effective. It exhibits remarkable properties. Thin coatings and nanoparticles represent practical applications of zinc phosphide, a *p*-type semiconducting diamagnetic substance with promising photovoltaic potential. This material exhibits a linear band-gap, making it highly suitable for single-junction solar cells, characterized by a band gap of around 1.5 eV.[4] The primitive tetragonal structure of Zn_3P_2 is characterized by the P42/nmc space group (No.137).[5] Gregory M. Kimball and his team[6] indicated that the optical absorption coefficient is significantly high (10^4-10^5 cm^{-1}), and the carrier diffusion length approaches 10 μm. The exploration and advancement of thin-film photovoltaic cells and various solar energy applications have captured the interest of researchers regarding zinc phosphide and its characteristics. In the context of recent investigations into the progress of half-metallic ferromagnetism and magnetic semiconductors, a considerable volume of experimental work remains to be undertaken on nano phases,[7-9] bulk materials,[10-11] and thin films.[12-14] These substances find application in photovoltaic technologies,[15] lithium/sodium ion energy storage systems,[16-18] and solar cell designs.[19-20] It is evident that the material Zn_3P_2 has received comparatively less attention in research, as indicated by the studies on Ti-doped Cd_3P_2,[21] Fe-doped Zn_3P_2,[22] and (S = V, Cr, Mn, Fe, Co) S-doped Zn_3P_2,[23] which were subsequently accompanied by ab initio analyses. A compound belonging to the II-V group of semiconductors is Zn_3P_2. The literature review focuses on the same set of compounds, which includes Mn-doped $ZnAs_2$,[24] $(Cd_{1-x}M_x)_3As_2$ alloys (M = Cr, Mn, Fe),[25] and Mn-doped Cd_3As_2.[26] The findings from the first-principles studies are subsequently detailed, showcasing features related to electronic structure, magnetism, and half-metallicity.

Our recent investigation focused on the optical, magnetic, and structural characteristics of Zn_3P_2 nanoparticles that have been doped with transition elements such as Fe, Ni, and Mn, employing the solid-state reaction method.[27-29] Research on non-magnetic dopants remain limited, despite the extensive investigation of transition-metal-doped Zn_3P_2 for its potential in magnetic and spintronic applications. The role of Sn inclusion in Zn_3P_2 nanopowders remain inadequately explored. The exploration of Sn as a non-magnetic dopant to enhance the structural, optical, and photoluminescence properties of Zn_3P_2 represents a novel contribution of this research. This study provides valuable insights into the emission processes induced by defects and the manipulation of the bandgap, aimed at improving the performance of Zn_3P_2-based optoelectronic devices.

The traditional solid-state reaction technique was employed to incorporate Sn into zinc phosphide nanoparticles in this study. This study examines the distinct characteristics of Sn-doped Zn_3P_2 through the substitution of different amounts of Sn (x = 0.03, 0.05, and 0.09) in place of zinc atoms. This study investigates the optical, photoluminescence, and structural properties of Sn: Zn_3P_2, revealing the effects of varying doping concentrations.

2. Experimental work

2.1 *Chemicals used*

Utilized were high-purity precursor materials, which required no additional purification. Zinc phosphide (Zn_3P_2, Sigma-Aldrich, ≥ 99.9%) and tin phosphide (SnP, Indiamart, ≥ 99.9%) served as the initial substances for the experiment. All the substances were in powdered form.

2.2 *Synthesis of Sn-doped Zn_3P_2 nanoparticles*

The conventional solid-state reaction technique was employed to synthesize Zn_3P_2 Nanoparticles (NPs) doped with Sn. Materials with different concentrations of Sn (x = 0.03 to 0.09) were employed for the preparation. Employing a stoichiometric ratio of $Zn_{(3-x)}Sn_xP_2$, where x is set to 0.03, 0.05, and 0.09, the compounds were quantified and measured. Initially, it is essential to utilize acetone for the cleaning of the mortar and pestle apparatus. Over a period of approximately 16 hours, the molecules comprising Sn-doped zinc phosphide were thoroughly milled. A fixed plate crucible made of alumina was utilized to contain the powder samples, which were crushed prior to being placed inside. Tube furnaces ensure ideal conditions for effective sampling. It is essential to

maintain the samples at a temperature of 500 °C for a duration of five hours, ensuring a vacuum level of 2×10^{-2} mbar. The samples underwent an extensive grinding process for three hours following sintering to ensure they were adequately prepared for characterisation. The final product of Sn-doped Zn_3P_2 nanoparticles exhibited a deep black appearance.

2.3 *Characterizations*

All synthesized materials underwent characterization through various methods to assess their structural, elemental, morphological, optical, and photoluminescence properties. The crystalline structure of the nanoparticles was examined using X-Ray Diffraction (XRD) (Rigaku MiniFlex 600) employing Cu Kα radiation (λ = 1.5406 Å) over a 2θ range of 20°-90° with a step size of 0.02°. Energy-Dispersive X-ray Spectroscopy (EDS) (AMETEK) was employed to assess elemental composition alongside the Scanning Electron Microscope (SEM) apparatus. The examination of surface morphology was conducted utilizing a SEM (JSM-IT500) operating at an accelerating voltage range of 10-20 kV. A Ultraviolet-Visible-Near-Infrared (UV-Vis-NIR) spectrophotometer (PerkinElmer Lambda 365) was employed to obtain diffuse reflectance spectra ranging from 200 to 1,100 nm, with the optical band gap estimated using the Kubelka-Munk function. Photoluminescence (PL) spectra were collected utilizing a fluorescence spectrometer (FP-8300) with an excitation wavelength set at 250 nm.

3. Results and discussions

3.1 *Structural properties*

Figure 1a presents the XRD patterns of both pure and Sn-doped zinc phosphide nanoparticles produced through a solid-state method. The XRD patterns of $Zn_{(3-x)}Sn_xP_2$ nanoparticles are presented for x values of 0.03, 0.05, and 0.09. All the samples exhibited the tetragonal Zn_3P_2 structure. The JCPDS cards, space group 137, and reference number 74-1156 aligned seamlessly. A similar configuration was identified by Stutz et al.[30] The presence of doped samples and Zn_3P_2 reveals distinct diffraction peaks, signifying a high level of crystallinity. The lack of additional peaks in the XRD pattern, as illustrated in Figure 1a, suggests that the pure (Zn_3P_2) was effectively doped with Sn, as no other impurities were detected.

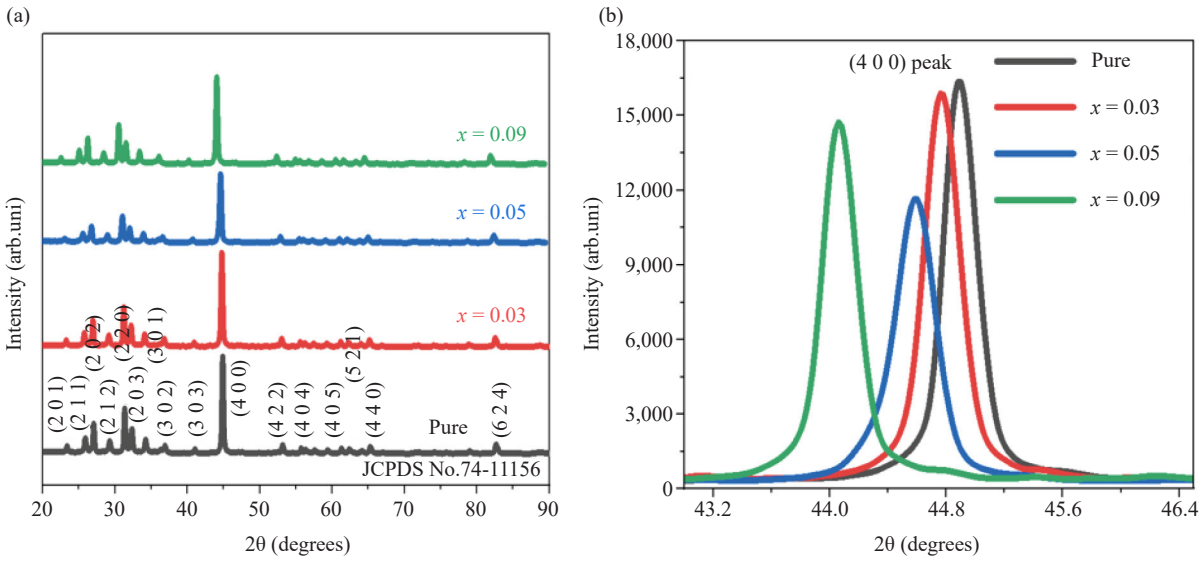


Figure 1. (a) XRD patterns of pure and $Zn_{(3-x)}Sn_xP_2$ samples (b) peak (4 0 0) in the range of 43.2°-46.4°

Figure 1b demonstrates the variation of 2θ, shifting from 43.2° to 46.4°. The difference in ionic radius, specifically between Zn^{2+} (0.74 Å) and Sn^{2+} (0.99 Å), results in a shift of the angle 2θ towards lower values as the concentration of the Sn dopant increases from x = 0.03 to 0.09 in the sample. Even with its larger ionic radius relative to Zn^{2+}, the Sn dopant incorporated into the Zn_3P_2 lattice is achieved effectively. Ni-doped Zn_3P_2 at reduced angles showed similar outcomes.[27] The average crystallite size (D) for all synthetic and pure samples from the (4 0 0) plane was determined using the Debye Scherrer equation.[31]

$$\text{Crystallite size } D = \frac{K\lambda}{\beta \cos\theta} \tag{1}$$

Through the analysis of observable peaks in both pure and doped samples, we can determine the average crystallite size, D, with a constant value of K being 0.9. The parameters λ for wavelength (Cu Kα, 0.15406 nm), 2θ for the diffraction angle of the primary peak (4 0 0), and β for the full-width at half-maximum of both pure and doped (4 0 0) peaks in X-ray diffraction are established. The crystallite dimensions reduced from 30.44 to 25.46 nm as the Sn concentration rose from x = 0.03 to 0.09, as illustrated in Table 1. External pollutants cause deformation in the host Zn_3P_2 lattice, which significantly contributes to the reduction in crystallite size.[29]

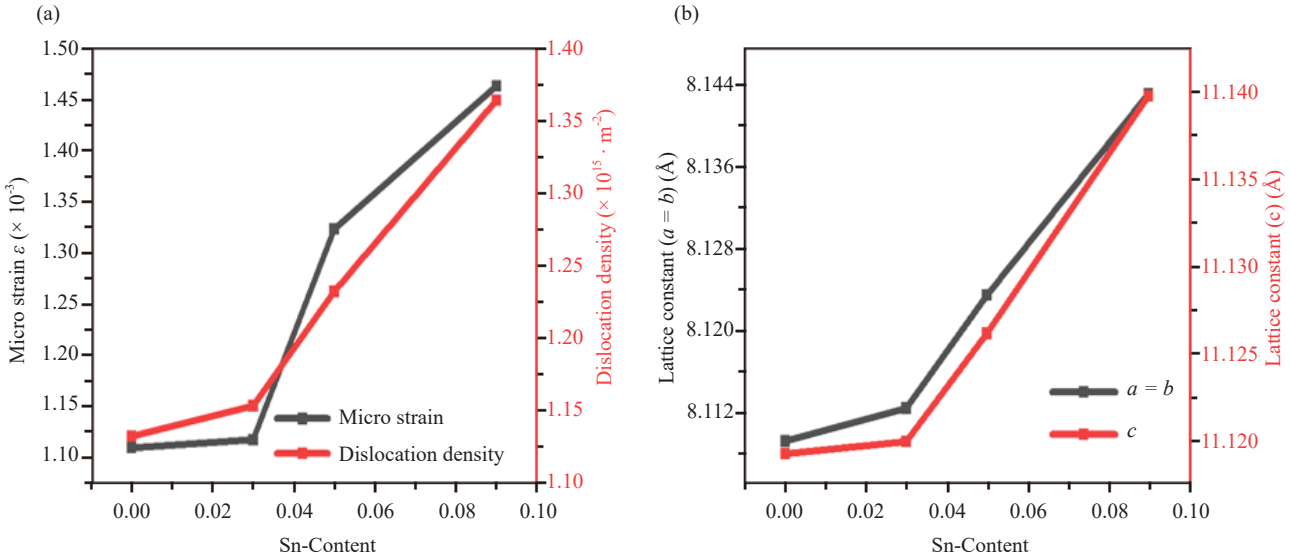


Figure 2. (a) Micro strain and dislocation density and (b) lattice parameters

Figure 2a illustrates the relationship among Sn concentration, microstrain, and dislocation density. The dislocation density (δ) in both pure and doped samples exhibits an inverse relationship with the square of the average crystalline scale (D), a relationship that can be utilized to identify imperfections in crystalline structures.[27]

$$\text{Dislocation density } \delta = \frac{1}{D^2} \tag{2}$$

The crystallite size, represented by D, is measured in nanometers. The dislocation density rises from 1.132 to 1.364 with higher Sn-concentration, as illustrated in Table 1. XRD can be employed to investigate microstrain and lattice distortions in crystalline substances. With the increase in Sn concentration, the microstrain escalated from 1.109 to 1.463, signifying lattice deformation induced by the incorporation of Sn ions into the Zn_3P_2 lattice. An estimation of the micro-strain (ε) can be derived using the formula presented below.[27]

$$\text{Micro-strain } \varepsilon = \frac{\beta \cos \theta}{4} \tag{3}$$

In the context of both pure and doped synthetic materials, θ denotes the angle of diffraction for the (4 0 0) plane, whereas β signifies the Full-Width Half Maximum (FWHM). An increase in dislocation density and microstrain can indicate the presence of various lattice defects. Figure 2b demonstrates the influence of Sn-content on the lattice characteristics. The tetragonal structure and the results from X-ray diffraction are utilized to derive the formula for estimating the lattice parameters of both pure and Sn-doped nanoparticles.[27]

$$\frac{1}{d^2} = \left(\frac{h^2 + k^2}{a^2} + \frac{l^2}{c^2} \right) \tag{4}$$

Bragg's equation specifies the interplanar distance ($d = n\lambda/2\sin\theta$), the ordering ($n = 1$), the wavelength of the incoming ray ($\lambda = 1.5406$ Å), and the diffraction angle (θ). The lattice parameters of the (4 0 0) diffraction plane exhibited an increase with rising Sn-content in both pure and doped materials, transitioning from $a = b = 8.1093$ Å to 8.1431 Å and $c = 11.1193$ Å to 11.1398 Å. An alteration in the ionic radii of the dopant Sn^{2+} and the host Zn^{2+} results in an increase in this lattice constant. This study demonstrated that the synthesized Zn_3P_2 crystal lattice readily incorporates Sn-ions at the Zn^{2+} site. Table 1 presents various X-ray diffraction characteristics, such as crystallite size, lattice dimensions, optical band gap, microstrain, dislocation density, and microstrain.

Table 1. Summarises the properties of XRD

System name	2θ (degree)	FWHM	Crystallite size D (nm)	a (Å)	c (Å)	Micro strain (10^{-3})	Dislocation density (10^{15}·m^{-2})	Bandgap (eV)
Pure	44.88	0.2734	30.44	8.1093	11.1193	1.109	1.132	1.422
Sn ($x = 0.03$)	44.76	0.2917	29.44	8.1125	11.1200	1.117	1.153	1.425
Sn ($x = 0.05$)	44.58	0.3276	26.20	8.1235	11.1262	1.323	1.232	1.429
Sn ($x = 0.09$)	44.06	0.3475	25.46	8.1431	11.1398	1.463	1.364	1.432

3.2 *Surface morphological studies*

Figure 3 illustrates instances of nanoparticles of Sn-doped Zn_3P_2 with concentrations varying from $x = 0.03$ to 0.09 within the 500 nm range. As the doping concentration increased in the pure system, the small aggregates developed into larger structures, and spherical forms emerged. The SEM images provided this indication. The concentration of dopants plays a pivotal role in influencing agglomeration; as the dopant concentration rises, the pure compound begins to occupy the atomic positions. The SEM images indicate that the diameters of the produced particles are measured at 125 nm, 148 nm, 168 nm, 240 nm, 287 nm, 302 nm, and 489 nm.

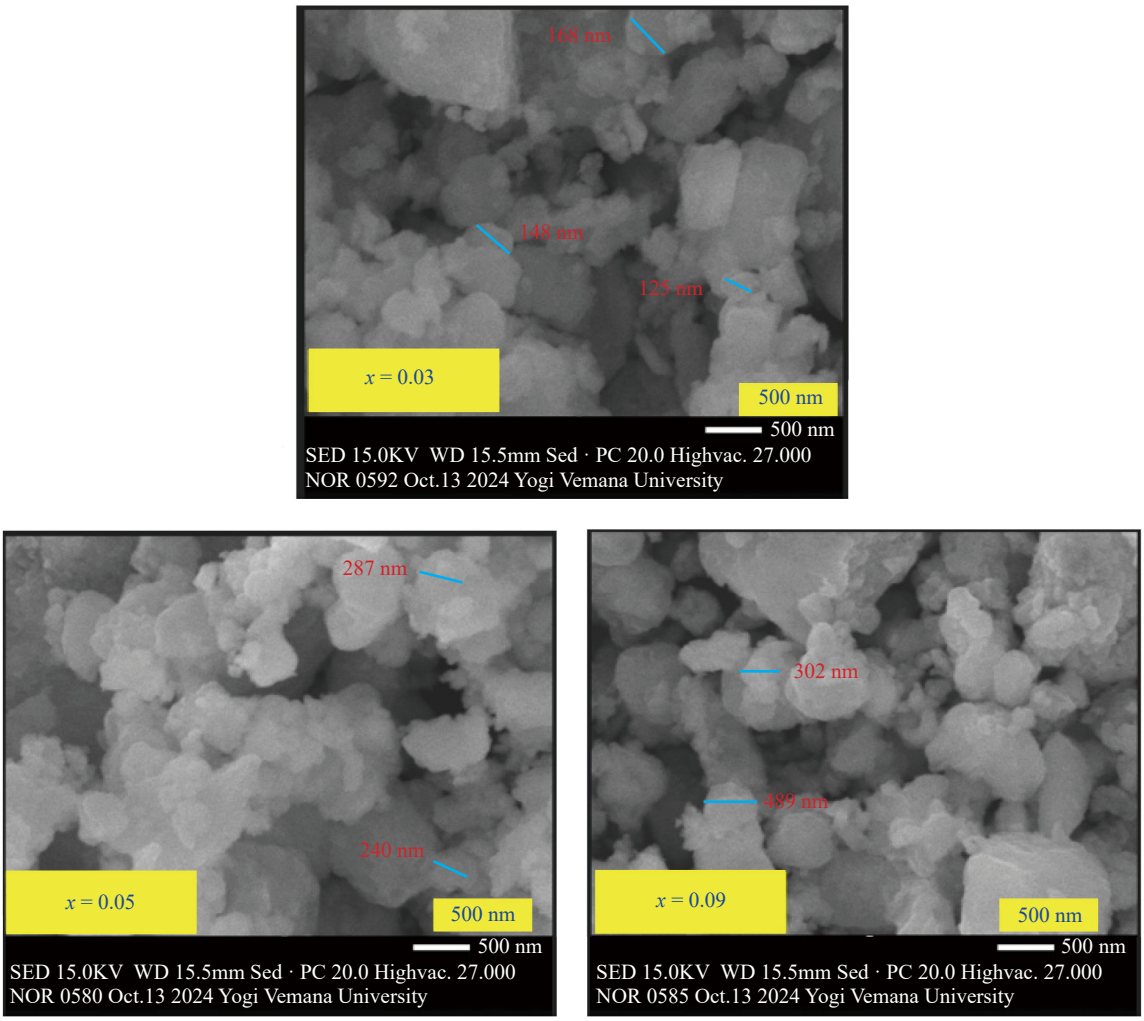


Figure 3. SEM images with Sn

3.3 *Elemental studies*

The elemental composition of $Zn_{(3-x)}Sn_xP_2$ (x = 0.03, 0.05, and 0.09) nanoparticles synthesized can be examined through energy-dispersive X-ray spectroscopy, as illustrated in Figure 4. Upon examining the spectra of Sn-doped Zn_3P_2 samples, it was found that the atomic ratios of zinc (Zn), phosphorus (P), and tin (Sn) closely matched the predicted values. EDS analysis demonstrated that the Sn-dopant ions were effectively incorporated into Zn_3P_2, and the X-ray diffraction data confirmed the absence of any additional contaminants.

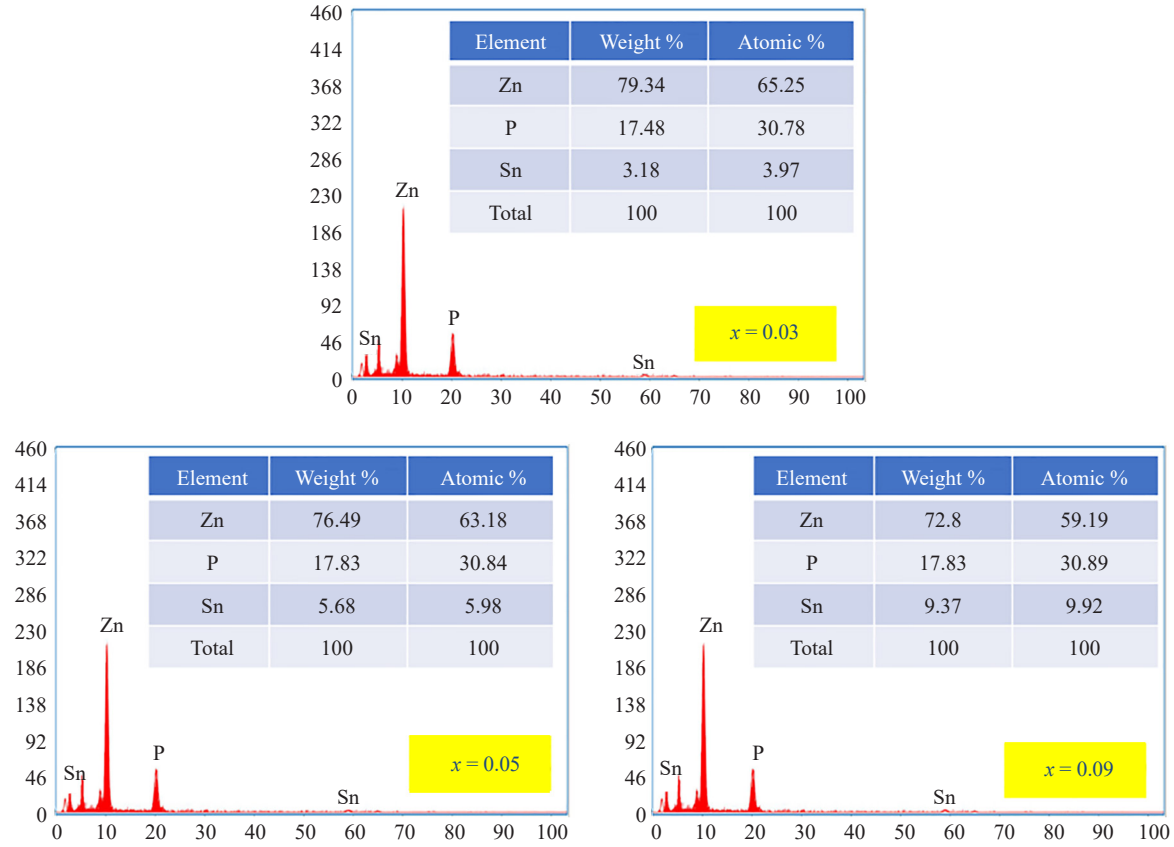


Figure 4. EDS spectra with Sn content

3.4 *Optical properties*

The optical characteristics of zinc phosphide nanoparticles, both with and without Sn doping, were investigated through the use of Diffuse Reflectance Spectra (DRS). Figure 5a shows the DRS of both undoped and Sn-doped nanoparticles at room temperature, covering a wavelength range from 200 nm to 1,100 nm. In the infrared region, the pure system exhibited the highest reflectivity at 54%, whereas the Sn-doped zinc phosphide nanoparticle samples showed the lowest reflectivity. The reflectance of $Zn_{(3-x)}Sn_xP_2$ nanoparticles increased with the rise in Sn concentration in the sample, moving from $x = 0.03$ to 0.09. Pure and Sn-doped materials undergo analysis through a $F(R)$ represented by the Kubelka-Munk function, calculated via the equation provided.[28]

$$F(R)=\frac{(1-R)^2}{2R} \tag{5}$$

In this context, R denotes the DRS, while $F(R)$ signifies the reflectance function. The Tauc equation[28] was employed to determine the optical band gap in both pure and synthetic materials.

$$\left(F(R)\cdot hv\right)^{1/n} = A(hv-E_g) \tag{7}$$

In the equation, $F(R) = \alpha$ signifies the absorption coefficient, hv denotes photon energy, v indicates light frequency, E_g refers to the optical band gap between the conduction and valence bands, and n is dependent on the nature of the transition and in the present case 'n' was taken 1/2 for a direct allowed transition.[29] To achieve this, the absorption coefficient graph can be extended from photon energy (hv) to the linear region ($\alpha = 0$). The pure and Sn-doped samples

displayed optical band gaps ranging from 1.30 to 1.60 eV, as illustrated in Figure 5b. The optical band gap for pure (Zn_3P_2) nanoparticles was determined to be 1.5 eV, consistent with earlier findings.[4] The optical band expanded from 1.422 to 1.432 eV as the Sn concentration increased from $x = 0.03$ to 0.09. The increase in dopant (Sn) concentration is demonstrated to result in a widening of the band gap. The optical band gap could potentially be expanded through the Burstein-Moss effect.[27] In a similar manner, $Zn_{3-x}Ni_xP_2$ nanoparticles synthesized through the solid-state method with x values of 0.01, 0.03, 0.05, and 0.07 exhibited a notable band gap expansion as Ni concentration increased post-doping, shifting from its original position in the conduction band of Zn_3P_2 semiconductors.[28]

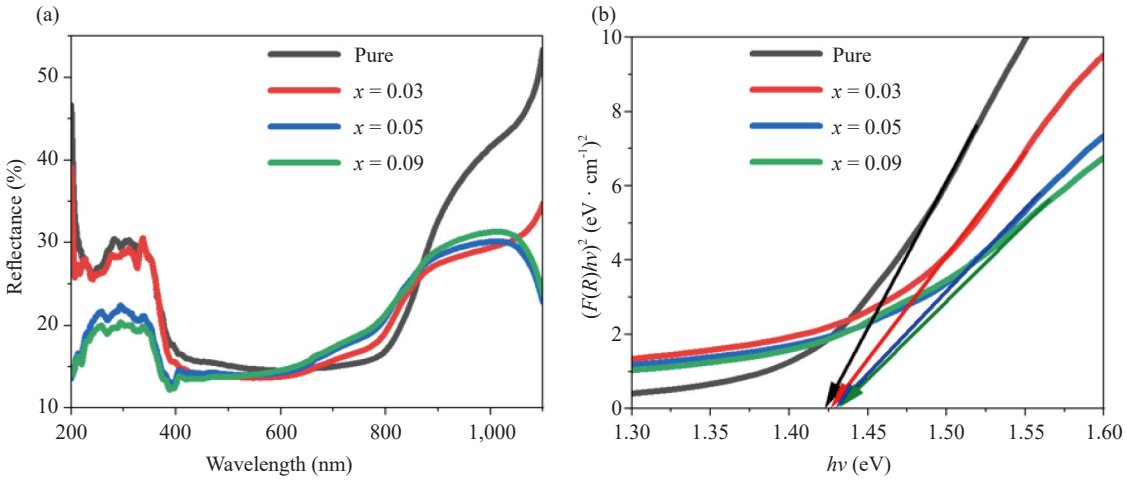


Figure 5. (a) DRS of pure and $Zn_{(3-x)}Sn_xP_2$ samples and (b) optical band gap

3.5 *Photoluminescence studies*

The characteristics of materials can be assessed through the use of PL spectroscopy. This method exhibits a remarkable sensitivity to recombination phenomena and defects in electronic structure. PL spectroscopy, being a contactless and non-destructive technique, is extensively utilized for the analysis of optoelectronic properties in semiconductors. The characteristics of emission and excitation peaks in photoluminescence spectra are influenced by the concentrations and energy levels of defects or electronic band transitions.

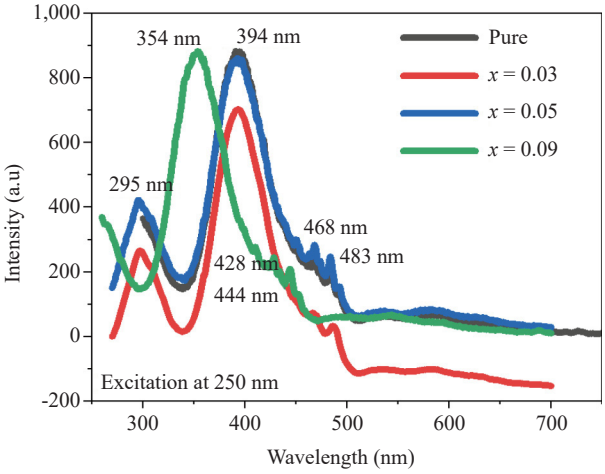


Figure 6. PL spectra of Sn-doped Zn_3P_2 nanoparticles

Figure 6 illustrates the photoluminescence spectra for both pure and Sn-doped Zn_3P_2 samples. The recording range spans from 245 nm to 750 nm, utilizing an excitation wavelength of 250 nm. The concentration of Sn influences the emission peaks observed in the PL spectra of Zn_3P_2 nanoparticles that have been doped with Sn. The emissions are observed in the ultraviolet (295 nm, 4.20 eV), near-ultraviolet/violet (354 and 394 nm, 3.50 and 3.14 eV), and blue (428, 444, 468, and 483 nm, 2.89, 2.79, 2.64, and 2.56 eV) regions. Weaker emission bands show up in the blue area at longer wavelengths, whereas the most noticeable emission peaks are seen between 354 and 394 nm. As the dopant concentrations increased from x = 0.03 to 0.09, the intensity increased concurrently. In the range of x = 0.03 to 0.05, the emission peak wavelengths of both the synthesized and the unmodified nanoparticles show a high degree of similarity. The emission peak at x = 0.09 appears to have shifted towards the lower angle side, potentially due to fluctuations in its electronic energy levels. These variations could be influenced by factors such as temperature, excitation wavelength, sample composition, size, and surface morphology. The linear band gap of zinc phosphide is measured at 1.5 eV. The band edges of all the produced nanoparticles differ from those of the bulk Zn_3P_2, as illustrated in Figure 5b. Surface defects in nanoparticles can lead to the formation of both superficial and deep traps beneath the conduction band.[29] Shen et al.[32] noted a wide emission peak at 585 nm (2.1 eV) in the photoluminescence spectra of single-crystalline trumpet-like Zn_3P_2 nanostructures. Teck Hock Lim and colleagues[33] observed PL emissions from α-Zn_3P_2 dispersed in solvent, showing peaks at 350 nm (3.5 eV) and 470 nm (2.6 eV) in butanol. Recent studies have focused on the comparison of transition metal-doped Zn_3P_2 nanoparticles for photoluminescence characterization.[28]

4. Conclusion

The $Zn_{(3-x)}Sn_xP_2$ (x = 0.03, 0.05, and 0.09) nanoparticles were synthesized using a solid-state reaction technique. A variety of characterization techniques are employed to assess phase, surface morphology, crystallite size, energy bandgap, and luminescence studies. The XRD patterns of all synthesized nanoparticles confirmed a single-phase tetragonal structure, showing no noticeable impurity peaks. As the concentration of Sn rises, both the microstrain and dislocation density show an increase, moving from 1.109 to 1.463 and from 1.132 to 1.364, respectively. The band gap energy exhibited a slight increase from 1.422 eV to 1.432 eV as the concentration of Sn was elevated. With excitation at 250 nm, the PL spectra demonstrated that both pure and Sn-doped nanoparticles primarily emit in the ultraviolet, violet, and blue regions.

Acknowledgment

We appreciate the PL facilities provided by IIT Madras.

Author contribution

NPK completed the writing, characterization, and synthesis. NPK, NMR, SVMS and MKM discussed the results and commented on the text.

Funding

No funding, money, or other assistance was obtained in the writing of this text, the author affirms.

Data availability

Upon reasonable request, data will be made accessible. This study's supporting data may be obtained from the

corresponding author upon reasonable request.

Ethical approval

There is no research conducted by any of the authors using humans or animals in this article. There were no human or animal samples taken for this experiment.

Conflict of interest

The authors of this work affirm that there isn't any conflict of interest.

References

[1] Parida, P.; Patra, J.; Singh, V. R.; Verma, V. K. Dilute Magnetic Semiconductors and Its Applications-An Overview. In *International Conference on Advanced Nanomaterials and Applications*; Springer Nature Singapore: Singapore, 2024; pp 181-220.

[2] Najafi, A. Magneto-Optical Studies of Group II-VI Diluted Magnetic Semiconductor Nanoplatelets. Ph.D. Dissertation, State University of New York at Buffalo, 2021.

[3] Kathiravan, P.; Thillaivelavan, K.; Viruthagiri, G. Mn doping nanoarchitectonics of NiO nanoparticles with various property impacts for optoelectronic devices and diluted magnetic semiconductor applications. *J. Mater. Sci.: Mater. Electron.* **2024,** *35*(31), 2012.

[4] Bhushan, M.; Turner, J. A.; Parkinson, B. A. Photoelectrochemical investigation of Zn_3P_2. *J. Electrochem. Soc.* **1986,** *133*, 536-542.

[5] Zanin, I. E.; Aleinikova, K. B.; Antipin, M. Y.; Afanas'ev, M. M. Analysis of chemical bonding in Zn_3P_2 crystals from X-ray diffraction data. *Crystallogr. Rep.* **2004,** *49*(4), 579-584.

[6] Kimball, G. M.; Müller, A. M.; Lewis, N. S.; Atwater, H. A. Photoluminescence-based measurements of the energy gap and diffusion length of Zn_3P_2. *Appl. Phys. Lett.* **2009,** *95*(11), 112103.

[7] Miao, S.; Yang, T.; Hickey, S. G.; Lesnyak, V.; Rellinghaus, B.; Xu, J.; Eychmüller, A. Emissive ZnO@ Zn_3P_2 nanocrystals: Synthesis, optical, and optoelectrochemical properties. *Small* **2013,** *9*(20), 3415-3422.

[8] Dzade, N. Y. First-principles insights into the interface chemistry between 4-aminothiophenol and zinc phosphide (Zn_3P_2) nanoparticles. *ACS Omega* **2020,** *5*(2), 1025-1032.

[9] Glassy, B. A.; Cossairt, B. M. Resolving the chemistry of Zn_3P_2 nanocrystal growth. *Chem. Mater.* **2016,** *28*(17), 6374-6380.

[10] Tiede, A.; Lemerle, R.; Hagger, T.; Rabelo, H.; Sampedro, M. T.; Spadaro, M. C.; Fontcuberta i Morral, A. Long-term protection of crystalline zinc phosphide (Zn_3P_2) under atmospheric conditions. *APL Mater.* **2026,** *14*(1), 011113.

[11] Stamov, I. G.; Syrbu, N. N.; Dorogan, A. V. Energetic band structure of Zn_3P_2 crystals. *Physica B* **2013,** *408*, 29-33.

[12] Sathyamoorthy, R.; Sharmila, C.; Natarajan, K.; Velumani, S. Influence of annealing on structural and optical properties of Zn_3P_2 thin films. *Mater. Charact.* **2007,** *58*, 745-749.

[13] El Zawawi, I. K.; Moez, A. A.; Hammad, T. R.; Ibrahim, R. S. Phase transformation and disorder effect on optical and electrical properties of Zn_3P_2 thin films. *Spectrochim. Acta, Part A* **2012,** *94*, 378-383.

[14] Zamani, M.; Stutz, E.; Escobar, S.; Zamani, R. R.; Paul, R.; Leran, J. B.; Fontcuberta i Morral, A. The path towards 1 μm monocrystalline Zn_3P_2 films on InP: Substrate preparation, growth conditions and luminescence properties. *J. Phys. Energy* **2021,** *3*(3), 034011.

[15] Escobar Steinvall, S.; Salutari, F.; Johansson, J.; Das, I.; Lehmann, S.; Church, S. A.; Dick, K. A. Interfaces in epitaxially grown Zn_3P_2 nanowires and their composition-dependent optoelectronic properties for photovoltaic applications. *Chem. Mater.* **2025,** *37*(15), 5805-5813.

[16] Li, X.; Li, W.; Yu, J.; Zhang, H.; Shi, Z.; Guo, Z. Self-supported Zn_3P_2 nanowires-assembly bundles grafted on Ti foil as an advanced integrated electrodes for lithium/sodium ion batteries with high performances. *J. Alloys Compd.* **2017,** *724*, 932-939.

[17] Bichat, M. P.; Pascal, J. L.; Gillot, F.; Favier, F. Electrochemical lithium insertion in Zn_3P_2 zinc phosphide. *Chem. Mater.* **2005,** *17*(26), 6761-6771.
[18] Li, W.; Gan, L.; Guo, K.; Ke, L.; Wei, Y.; Li, H.; Zhai, X. Self-supported Zn_3P_2 nanowire arrays grafted on carbon fabrics as an advanced integrated anode for flexible lithium ion batteries. *Nanoscale* **2016,** *8*(16), 8666-8672.
[19] Adul, J. A.; Eya, H. I.; Mishra, N.; Dzade, N. Y. DFT Insights into the optoelectronic, valence band photoemission spectra, and interface band alignment properties of Zn_3P_2 solar absorber. *Mater. Today Commun* **2025,** *49*, 114275.
[20] Babu, P. S.; Singh, P. K.; Thakur, A. K.; Dwivedi, D. K. Optimization of photovoltaic solar cell performance via the earth abundant Zn_3P_2 back surface field. *Optik* **2021,** *229*, 166235.
[21] Jaiganesh, G.; Jaya, S. M. Electronic structure and magnetism of titanium substituted Cd_3P_2: An *ab-initio* study. *AIP Conf. Proc.* **2018,** *1953*(1), 120062.
[22] Jaiganesh, G.; Mathi, J. S. Half-metallic ferromagnetism in Fe-doped Zn_3P_2 from first-principles calculations. *AIP Conf. Proc.* **2014,** *1591*, 1081-1083.
[23] Jaiganesh, G.; Jaya, S. M. Magnetism, electronic structure and half-metallic property of transition metal (V, Cr, Mn, Fe, Co) substituted Zn_3P_2 dilute magnetic semiconductors: An *ab-initio* study. *Comput. Mater. Sci.* **2015,** *102*, 85-94.
[24] Kochura, A.; Fedorchenko, I.; Laiho, R.; Lashkul, A.; Lähderanta, E.; Marenkin, S.; Zakharov, I. Growth and magnetic properties of Mn-doped $ZnSiAs_2$/Si heterostructures. *Phys. Status Solidi C* **2009,** *6*(5), 1336-1338.
[25] Kulatov, E. T.; Uspenskii, Y. A.; Kugel, K. I. Magnetic topological alloys based on the Cd_3As_2 dirac semimetal: Doping with Cr, Mn, and Fe. *JETP Lett.* **2025,** *121*(9), 735-745.
[26] Xiao, R.; Held, J. T.; Rable, J.; Ghosh, S.; Wang, K.; Mkhoyan, K. A.; Samarth, N. Challenges to magnetic doping of thin films of the Dirac semimetal Cd_3As_2. *Phys. Rev. Mater.* **2022,** *6*(2), 024203.
[27] Praveenkumar, N.; Rao, N. M. Room temperature ferromagnetism in undoped and Fe doped Zn_3P_2 nanoparticles: Structural, optical and magnetic properties. *Solid State Sci.* **2024,** *151*, 107519.
[28] Praveenkumar, N.; N, M. R. Ni doped Zn_3P_2 nanoparticles: Synthesis, structural, optical, and magnetic properties. *J. Supercond. Novel Magn.* **2024,** *37*(1), 165-177.
[29] Praveenkumar, N.; Madhusudhana Rao, N. Synthesis of (Mn, Fe) Co-doped Zn_3P_2 nanoparticles: Structural, optical and magnetic properties via solid-state reaction route. *J. Mater. Sci.: Mater. Electron.* **2024,** *35*, 719.
[30] Stutz, E. Z.; Escobar Steinvall, S.; Litvinchuk, A. P.; Leran, J. B.; Zamani, M.; Paul, R. Raman spectroscopy and lattice dynamics calculations of tetragonally-structured single crystal zinc phosphide (Zn_3P_2) nanowires. *Nanotechnology* **2021,** *32*(8), 085704.
[31] Cullity, B. D. *Elements of X-Ray Diffraction*; Addison-Wesley: Reading, MA, USA, 1978.
[32] Shen, G. Z.; Bando, Y.; Hu, J. Q.; Golberg, D. Single-crystalline trumpetlike zinc phosphide nanostructures. *Appl. Phys. Lett.* **2006,** *88*(14), 143105.
[33] Lim, T. H.; Teh, G. B.; Tilley, R. D. Synthesis and characterization of highly crystalline zinc phosphide nanoparticles. *Key Eng. Mater.* **2016,** *701*, 3-7.